Article

Journal of the Brazilian Chemical Society

https://dx.doi.org/10.21577/0103-5053.20240105

J. Braz. Chem. Soc. **2024**, *35*, 12, e-20240105, 1-12

Detection of Psychoactive *N*,*N*-Dimethyltryptamine Alkaloid Based on Surface-Enhanced Raman Scattering Using Gold Nanostars in Flexible Inkjet-Printing Paper Substrates

Edison Huertas-Montoya, [a] ***Anerise de Barros,*** [a] ***Lucas M. F. Oliveira,*** [a] ***Paola A. Caro Aponte,*** [b] ***Alexandre L. R. Oliveira,*** [b] ***Flavio M. Shimizu,*** [c,d] ***Alessandra Sussulini,*** [e] ***Fernando A. Sigoli*** [a] ***and Italo O. Mazali*** *,[a]

[a]*Laboratório de Materiais Funcionais, Instituto de Química, Universidade Estadual de Campinas, 13083-970 Campinas-SP, Brazil*

[b]*Laboratório de Regeneração Nervosa, Instituto de Biologia, Universidade Estadual de Campinas, 13083-862 Campinas-SP, Brazil*

[c]*Instituto de Física Gleb Wataghin, Universidade Estadual de Campinas, 13083-859 Campinas-SP, Brazil*

[d]*Laboratório Nacional de Nanotecnologia, Centro Nacional de Pesquisa em Energia e Materiais, 13083-100 Campinas-SP, Brazil*

[e]*Laboratório de Bioanalítica e Ciências Ômicas Integradas, Instituto de Química, Universidade Estadual de Campinas, 13083-970 Campinas-SP, Brazil*

N,*N*-Dimethyltryptamine (DMT) is a serotonergic psychedelic that, when combined with monoamine oxidase enzyme inhibitors in the hallucinogenic beverage commonly known as ayahuasca, surpasses most common orally administered psychoactive drugs. There is a growing interest in the therapeutic potential of DMT due to recent clinical data showing the improvement of cognitive deficits associated with depression and Alzheimer's disease. The development of analytical methodology for the monitoring of concentrations of DMT molecules to control the appropriate dosage for their use is essential for the treatment of patients. For this, we propose a novel flexible inkjet-printed paper substrate based on Au nanostars as proof of concept for DMT detection by surface-enhanced Raman scattering (SERS). The substrate was applied to detect DMT in water as a first approach to more complex matrices like ayahuasca beverages or blood samples. The optimization and performance of SERS substrates with different print cycles indicate that one print is enough to achieve the great performance of the flexible paper substrates. The SERS analyses for DMT in different concentrations, 10^{-3} to 10^{-10} mol L^{-1}, reveal a high sensitivity of the sensors with a silhouette coefficient of 0.84 obtained by principal component analysis (PCA) statistical projections.

Keywords: SERS, paper-based sensor, inkjet-printing, plasmonic nanoparticles, *N*,*N*-dimethyltryptamine

Introduction

N,*N*-Dimethyltryptamine (DMT) is an indole alkaloid commonly present in South American biota such as *Mimosa tenuiflora*, typical of the semi-arid areas of Brazil.[1,2] DMT is known to be a strong serotonergic psychedelic capable of producing experiences that, when combined with monoamine oxidase enzyme (MAO) inhibitors, can surpass those associated with standard doses of most orally administered psychoactive drugs.[3] This activity can be explained since DMT has a similar structure to serotonin (5-HT), allowing DMT to act as a strong agonist of the 5-HT_2A receptor, responsible for causing hallucinogenic effects.[3-5] Furthermore, DMT can be classified as an endogenous agonist of the sigma-1 receptor and several studies suggest that DMT-mediated sigma-1 receptor activity may induce (*i*) neuronal plasticity changes,[6-10] (*ii*) protection against cytotoxic perinatal brain

*e-mail: mazali@unicamp.br
Editor handled this article: Célia M. Ronconi (Associate)
Our tribute to Prof Oswaldo Luiz Alves for his contribution to science, exemplary work, profound wisdom, and unwavering determination.

injury and ischemic neurodegeneration in the neonatal striatum[11-14] and (*iii*) anti-inflammatory brain effects.[14,15]

DMT is not orally active due to its rapid degradation by monoamine oxidase enzyme type A (MAO-A). Then, it is usually combined with MAO inhibitors from other plants, like in the case of the potent hallucinogenic beverage commonly known as ayahuasca.[4,16,17] The effects of consuming ayahuasca have been variously summarized as inducing intense modifications in cognition, perception, and emotion, with a combination of stimulatory and visual psychoactive effects of longer duration and milder intensity than those previously reported for DMT administered in other ways.[7,10,17] Interestingly, ayahuasca and DMT represent an issue of relevance to health and well-being as they could be potentially employed for the treatment of physical and psychological disorders and to have a higher understanding of the action of psychedelics in the brain.[5,12,16] Recent clinical data[18] has demonstrated that ayahuasca produces antidepressant effects in humans that resemble the effects of fast-acting ketamine. Therapeutic use of ayahuasca suggests that it can have prolonged anxiolytic, antidepressant, and anti-addictive effects and is also considered safe.[12]

On the other hand, it has also been found that psychedelics that possess the central structure of DMT may have value as medications and cannot simply be labeled as drugs with the potential for abuse. These include triptans such as sumatriptan, rizatriptan, and zolmitriptan, which are compounds that are widely prescribed to treat migraines and cluster headaches.[4,18] The latter compounds are still in the experimental phase but have proven very promising in pre-clinical models concerning the improvement of cognitive deficits associated with depression and Alzheimer's disease.[19]

In this sense, the detection of DMT is not only important because of its use as a banned molecule but also because of its possible use as a therapeutic substance and the study of its role in neurological processes. Thus, considering that DMT interacts with serotonin receptors in the nanomolar range[20] the challenge comes in detecting low concentrations of DMT in complex mixtures that allow evidence of their function in these metabolic processes. Several instrumental methods to detect and quantify DMT have been reported, including high-performance liquid chromatography and gas or liquid chromatography coupled with mass detectors, among others.[1,2,17,20-23] However, these methods require pretreating the sample, time-consuming processes, and bulky workstations that are not suitable for field applications.

In this context, surface-enhanced Raman scattering (SERS) is an analytical technique that offers enhancement of the Raman intensity that is several orders of magnitude greater than the normal Raman signal of the isolated molecule, increasing the limits of detection.[24,25] The enhancement takes place at a metal surface, where molecules can undergo the improvement of Raman scattering through two main mechanisms. The electromagnetic mechanism is related to the localized surface plasmon, and the chemical effect mechanism is related to interactions between the molecule and the plasmonic surface that produce the charge transference between the molecule and the metal nanoparticles.[26,27] Furthermore, using the appropriate SERS substrate in the presence of hot spots, the enhancement of the Raman signal of the molecule increases more, even reaching single-molecule limits of detection.[28,29] Then, apart from the extremely high sensitivity, this technique also has other advantages, such as selectivity, due to the spectroscopic fingerprint, which makes it possible to perform multiplex detection.[30,31] Besides, the measurements are very fast and non-invasive, and the sample does not require any pre-treatment.[32,33]

Likewise, to design a high-performance SERS substrate, it must be economically viable, stable, and highly reproducible in terms of SERS activity. Considering this, inkjet printing on paper is a method based on the production of ink composed of metal nanoparticles, which are deposited on paper with the aid of a standard printer.[34] The deposition method has the advantage of low cost and simplicity, and the possibility of performing the substrate design using simple software.[35] Moreover, the use of paper as a substrate for sensor devices has advantages such as being from renewable sources, low cost, high commercial availability, ease of transport and storage, and biocompatibility due to cellulose.[36] For instance, Duan *et al.*[37] fabricated impressed Ag nanoparticle paper substrates for SERS detection of thiram fungicide. The substrate performance was evaluated by inkjet printing silver nanoparticles ink on four different papers (photographic, graph, weighing, and printing paper) with different wettability and different dried temperatures (90-120 °C). Hydrophobic papers (photographic, graph, and weighing paper) exhibited good uniformity and reproducibility, with a higher number of nanoparticles *per* spot diameter. Results show that the highest SERS activity was achieved for the Ag nanoparticles-photographic paper dried at 110 °C with the highest contact angle value, reaching a limit of detection (LOD) of ca. 10^{-10} mol L^{-1}.

Tay *et al.*[36] designed a paper-based SERS substrate made of 80 nm Au nanoparticles deposited into chromatography paper through drop-cast and inkjet-printing methods. As expected, the inkjet printing method leads to a more homogenous distribution of the nanoparticles above

the paper surface compared to the drop-cast method. However, it has the drawback that the amount of Au nanoparticles deposited in one single print pass is limited, requiring multiple printing steps to increase the number of nanoparticles *per* spot, the probability of hot spot regions, and, consequently, the enhancement of the SERS activity. The performance of the substrate was evaluated in the detection of benzenthiol reaching a LOD of 10^{-8} mol L^{-1} for six printing cycles.

Recently, our group[38] fabricated a hydrophobic paper substrate with enhanced SERS capabilities by the inkjet-printing method, combining Au nanospheres ink with a hydrophobic paper based on surface-modified chromatography paper. The inkjet-printed SERS substrate was applied for the detection and quantification of thiram, allowing quantification up to 10^{-11} mol L^{-1}.

In general, inkjet-printed SERS substrates reported in the literature[38-41] so far are based on silver or gold nanospheres and have been applied for the detection of pesticides and organic pollutants in the liquid phase, showing great results with limits of detection between 10^{-8}-10^{-12} mol L^{-1}. However, Tian *et al.*[42] have reported that for suspensions of equal nanoparticle and dye concentration, the SERS effect increases as nanospheres < nanosphere aggregates < nanotriangles < nanostars, clearly indicating that control over the number of local field "hot spots" can optimize the SERS efficiency. Therefore, we propose a novel flexible inkjet-printed paper SERS substrate using metallic nanostructures with other morphologies, specifically gold nanostars (Au NSs), as a proof of concept for drug detection using flexible inkjet-printed paper SERS substrates. Moreover, there are very few works reporting Raman or SERS detection of DMT or its derivate.[43-45] Hence, the Au NSs inkjet-printed paper SERS substrate was applied to detect DMT in water and as a first approach to more complex matrices like ayahuasca beverages or blood samples. For this, we evaluated the inkjet-printed SERS substrates with four different printing cycles, 1, 3, 5, and 10 prints, to demonstrate how the number of prints influences the SERS signal intensity. The use of Au NSs combined with the optimized number of printing cycles is the key feature of this work to achieve DMT detection up to 10^{-10} mol L^{-1}, as well as SERS substrates of low cost and easy commercialization. Excellent SERS performance and reproducibility were observed for the Au NSs inkjet-printed with only one print in the detection of crystal violet and DMT. The contact angle confirms the loss of hydrophobicity of inkjet-printed paper as a function of the number of printing cycles. Finally, the statistical analysis projection was taken to better evaluate the DMT SERS detection for different concentrations.

Experimental

Reagents and solutions

For the synthesis of the gold nanostars (Au NSs), hydrogen tetrachloroaurate(III) trihydrate ($HAuCl_4.3H_2O$, ≥ 99.9%), cetyltrimethylammonium bromide (CTAB, ≥ 99%), trisodium citrate dihydrate (≥ 98%), L-ascorbic acid (≥ 99%), silver nitrate ($AgNO_3$ ≥ 99%) and chloridric acid (37%) were purchased from Sigma-Aldrich (USA). For the paper functionalization, cellulose chromatographic paper (Whatman 30001-861), (2-dodecen-1-yl)-succinic anhydride (DDSA, 95%), and 1-hexanol (98%) were purchased from Sigma-Aldrich (USA). For the Au NSs ink, glycerol (≥ 99.5%) and absolute ethanol (99.5%) were purchased respectively from Sigma-Aldrich (USA) and Anidrol (Brazil), respectively. Crystal violet (CV) was purchased from Sigma-Aldrich (USA). All chemicals were of analytical grade and used without further purification.

Characterization

The morphology of the Au NSs was confirmed by transmission electron microscopy (TEM) using a Libra-Zeiss microscope (Germany) operating at 120 KV with a tungsten filament. The samples were prepared by dropping an aliquot of 5 μL of the Au NSs washed solution in a copper grid containing a carbon film (TedPella, USA). The optical properties of the Au NSs suspension and the final ink were studied by ultraviolet-visible (UV-Vis) spectroscopy in a Spectrophotometer Agilent Cary 50 (USA), using a quartz cuvette with a path length of 1 cm. The spectra were recorded between 200-1100 nm. The viscosity measurements were carried out on a HAAKE MARS III rheometer, Thermo Fisher Scientific (USA), equipped with a DG41 double-gap geometry. The measurements of flow curves were obtained in controlled rate mode with a shear rate of 10 up to 300 s^{-1} at 25 °C. The inkjet-printed substrates were examined with a Quanta FEG 250 field emission scanning electron microscope (FEI Co., USA) at low vacuum mode (10 Pa water vapor) operated at 10 kV using a solid-state detector for imaging of backscattered electrons (BSE). To study the optical properties of the inkjet-printed SERS substrate, diffuse reflectance spectroscopy (DRS) was recorded using a Shimadzu UV-2450 spectrophotometer (Japan).

N,*N*-Dimethyltryptamine extraction

DMT was extracted using *Mimosa tenuiflora* roots through an acid-to-base protocol, as reported by

e Amariz *et al*.[1] and Gaujac *et al*.[23] The purity of the isolated compound was confirmed by mass spectrometry (Figure S1, Supplementary information (SI) section) and ^{1}H nuclear magnetic resonance (^{1}H NMR) (Figure S2, SI section) techniques, obtaining a purity higher than 95%, which enabled the extracted compound to be used as a standard molecule for further detection using SERS (all the data related to the characterization of DMT can be found in the SI section).

Gold nanostars synthesis

The synthesis of the Au NSs was performed in two steps by combining the seed preparation method reported by Wuithschick *et al*.,[46] and the seed-mediated growth method reported by Ma *et al*.[47] Firstly, 7.5 mL of 1% m/m sodium citrate were added to a 50 mL boiling aqueous solution of $HAuCl_4$ (1 mmol L^{-1}). It was left boiling for an additional 15 min until the solution turned red wine, then cooled to room temperature and stored for further use. TEM images for seed characterization are shown in Figure S3b (SI section). Then, for the Au NSs growth, 50 µL of $HAuCl_4$ (50 mmol L^{-1}), 10 µL of HCl (1 mol L^{-1}) were added to 10 mL of seed solution (the reaction was carried at room temperature and the amount of seed was varied to modulate the length of the tips), then 10 µL of $AgNO_3$ (20 mmol L^{-1}) and 50 µL of ascorbic acid were simultaneously added under stirring for 10 min. Finally, 100 µL of CTAB (100 mmol L^{-1}) was added to the solution and stirred for another 10 min. The solution was centrifuged to wash the CTAB excess and redispersed in 10 mL of ultrapure water.

Fabrication of the Au NSs inkjet-printed SERS substrate

First, as shown in Figure S4 (SI section) the surface of the chromatography paper was functionalized with a hydrophobic layer of DDSA as follows, a sheet of chromatographic paper was immersed into 50 mL of DDSA (0.5% m/v) in 1-hexanol for 5 min and cured for 6 min at 160 °C. This process was repeated one time for each paper.[38] The contact angle (CA) of the functionalized and non-functionalized chromatography paper was measured in triplicate for each impression cycle using an optical tensiometer, Theta L (results are shown in Figure S5, SI section). The viscosity of the Au NSs solution was adjusted to be as close as possible to the commercial black ink EPSON 544 (Brazil) (Figure S6, SI section). Then, the final ink was prepared by mixing a suspension of Au NSs with glycerol and ethanol in a volume ratio of 65:25:10 respectively, and deposited on the functionalized paper, using a commercial printer EPSON L3110 (Brazil). Moreover, the number of printing cycles and the spot size and shape were optimized in order to obtain the highest SERS signal and reproducibility among measures. All data treatment was performed using Origin software.[48]

Raman and SERS measurements

The Raman and SERS spectra were collected using a HORIBA Scientific XploRA ONE Raman spectrophotometer coupled with a confocal microscope Jobin Yvon and a charge-coupled device detector (France). The measures were recorded with an excitation laser of 785 nm, 20 s of acquisition, 1 accumulation, and an objective lens of ×10. Two different power densities were used corresponding to 10 and 50% of the total power of the laser (4.5 and 22.8 mW, respectively). The results presented in the main article and in the SI section correspond to the 10% filter.

Statistical projections treatment

The analyses of Raman spectra were performed with linear and nonlinear multidimensional projection techniques, which are principal component analysis (PCA)[42] and interactive document mapping (IDMAP),[49] respectively. The raw dataset was first corrected by smoothing, denoising, and extended multiplicative scatters correction (EMSC) to decrease the data dispersion, a common effect observed in spectroscopic experiments. Then, the whole spectra (355 to 1700 cm^{-1}) were dimensionally reduced from 335 to 2 or 3 dimensions using FastMap or PCA algorithms, and the dissimilarities were calculated through Euclidean distance. Silhouette coefficient values were used as a metric to determine the discrimination quality.[50,51] All the analyses were performed in Python.[52]

Results and Discussion

Au NSs ink characterization

To produce an amount of ink enough to fill the printer tank, large quantities of nanoparticles are required. Hence, the synthesis was escalated from 10 to 500 mL, and several batches of Au NSs were prepared and concentrated to obtain 40 mL of ink (65% Au NSs/25% glycerol/15% ethanol) with a $[Au^0]$ = 27 mmol L^{-1}. The UV-Vis spectra in Figure 1a reveal a broad band centered at 690 nm characteristic of tips in branched structures and a second overlap band around 530 nm characteristic of the spherical core. After

preparation of the Au NSs ink, a small redshift is observed for both bands due to the change in solvent, entailing a change in the refractive index medium. Corroborated with this result, the branched morphology was confirmed by TEM, as shown in Figure 1b. It is observed that most of the Au nanoparticles have branches with a few irregular structures caused by the escalation process; we suggested that this occurs due to kinetic factors. Additional UV-Vis spectra and TEM images for Au seed and Au NSs synthesis optimization were inserted in the SI section (Figures S3a-S3f).

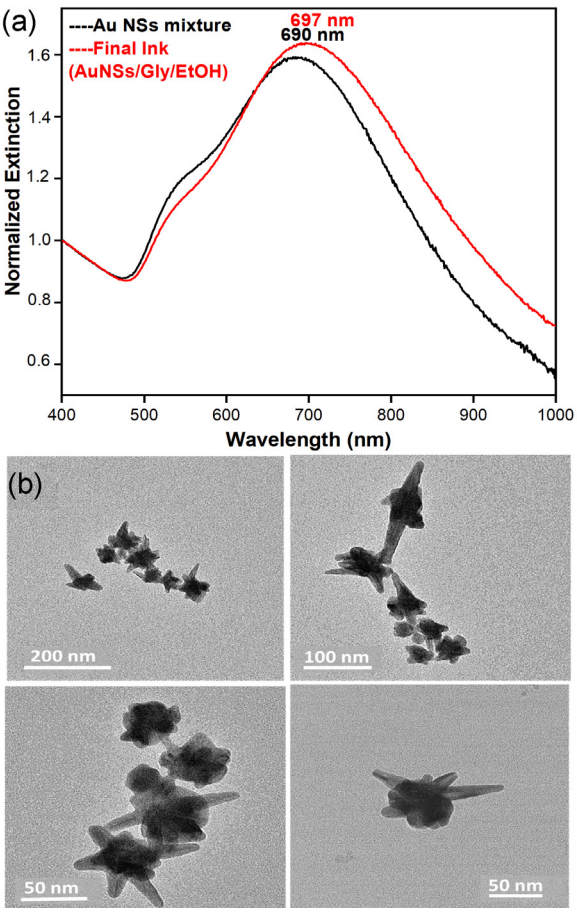

Figure 1. (a) UV-Vis spectra of the Au NSs suspension and final ink. The spectra were normalized by the absorbance value at 400 nm. (b) Au NSs TEM images at different magnifications.

Additionally, the stability of the final ink and the inkjet-printed substrate were investigated by spectroscopy and DRS, respectively, as shown in Figures 2a-2b. The results for the Au NSs ink (Figure 2a) reveal a significant redshift for the band at 697 to 627 nm up to 90 days, indicating poor stability of Au NSs in this storage condition. On the other hand, the printed Au NSs substrate is characterized by a single broadband at 548 nm. The significant shift compared to the Au NSs ink can be associated with the adsorption of Au NSs on paper fibers, favoring three-dimensional aggregation along the fibers. Despite the significant shift in optical properties between Au NSs ink and Au NSs printed substrate, the Au NSs printed substrate has excellent stability compared to the Au NSs ink which is a very important feature, especially when targeting commercial applications.

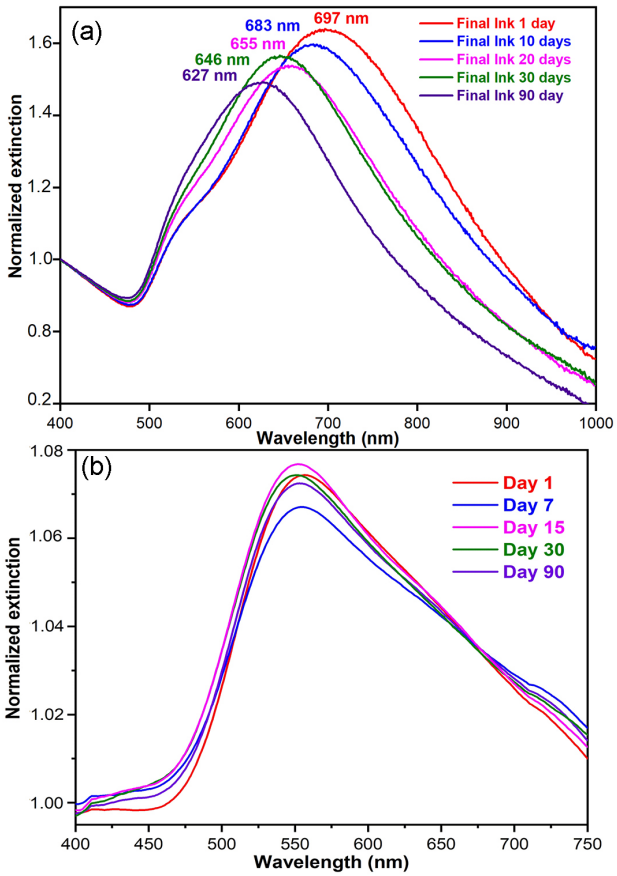

Figure 2. (a) UV-Vis spectra of the Au NSs final ink along the time. The spectra were normalized by the absorbance value at 400 nm. (b) Diffuse reflectance spectra of the 10 prints Au NSs substrate along time.

Au NSs inkjet-printed substrates characterization

The Au NSs distribution on the paper substrates for different printing cycles was characterized by SEM. Figures 3a-3d shows SEM images for 1, 3, 5, and 10 prints at two different magnifications. As expected, with the increase in the number of printings (Figure 3a: 10 prints), there is an increase in the surface coverage compared to lower printing cycles (Figures 3b-3d). In addition, the printing process shows good accuracy with a well-defined boundary, except for 1 print (Figure 3d). Thus, in order to evaluate the SERS performance based on the surface coverage for different printing cycles, we used CV as a probe molecule. For this, 2 µL of CV (10^{-5}

mol L^{-1}) were dropped and dried on the surface of the inkjet-printed spot, and then a set of three hundred SERS spectra were collected for every printing cycle (1, 3, 5, and 10 prints), the SERS maps and band assignment of the SERS spectrum of CV deposited on the Au NSs inkjet-printed paper substrate are shown in Figures S7 and S8 (SI section), respectively.

Note in Figure 3e that the highest SERS enhancement was achieved for the paper with one print, making it a very promising flexible SERS substrate since most of the reported works in the literature are based on spherical nanoparticles that require multiple prints.[35,37,46-48] This behavior is mainly related to the loss of the paper surface hydrophobicity. In this way, the hydrophobicity loss as a function of the number of prints is in agreement with contact angle measurements, as shown in Figure 4b. Note that for 1 and 3 prints, the average contact angle is ca. 110°, while a fall to 92 and 91° is observed for 5 and 10 prints, respectively. Thus, the decrease in the contact angle results in a decrease in paper hydrophobicity, allowing the water to spread out of the designed spot more easily. This wettability increase could be explained by the increase in glycerol content with the consecutive printing cycles, which allows water penetration on the substrate due to the high affinity between the hydroxyl groups of glycerol and water. To confirm this, the wettability of the paper substrates was studied by printing with a blank ink containing only water, glycerol, and ethanol. Different printing cycles (1, 3, 5, and 10) were evaluated by CA measures as shown in Figure 4a, in comparison with the functionalized paper without any printing there is a decrease of the CA values for all the printing cycles. Moreover, for 1 and 3 prints the CA values are pretty close 108 and 111°, respectively. However, for 5 and 10 prints there is a drastic decrease in the hydrophobicity of the paper surface 93 and 81°, respectively. These results are in agreement with the observed for the Au NSs inkjet-printed substrates, showing how the increase in the number of printing cycles affects the hydrophobicity, consequently, decreasing the SERS intensity even for higher amounts of nanoparticles, due to a lower number of molecules interacting with the surface of the printed spots. Besides, as reported by Solís *et al.*[53] regardless of the surface coverage for Au nanoparticle monolayers with different morphologies, Au NSs show a higher SERS intensity enhancement compared to nanosphere or nanorod morphologies. Hence, the SERS intensity decreases with the increase in the number of printing cycles due to the formation of aggregates that lead to the loss of the plasmonic properties and the convergence to the metallic bulk properties.

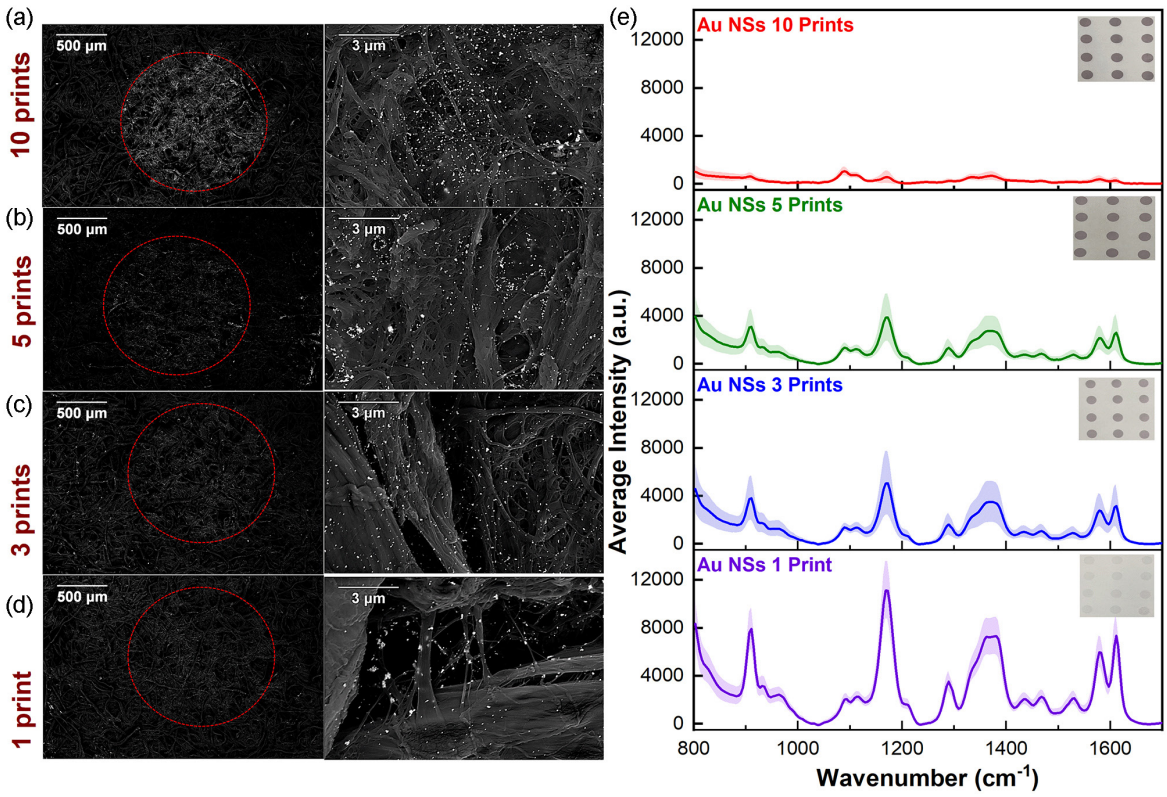

Figure 3. (a-d) SEM images for 10, 5, 3, and 1 printing cycles. The dashed red line represents the boundary of the printed circular spots of 1 mm diameter. (e) SERS average spectra of CV (10^{-5} mol L^{-1}) deposited on the Au NSs substrates with different printing cycles.

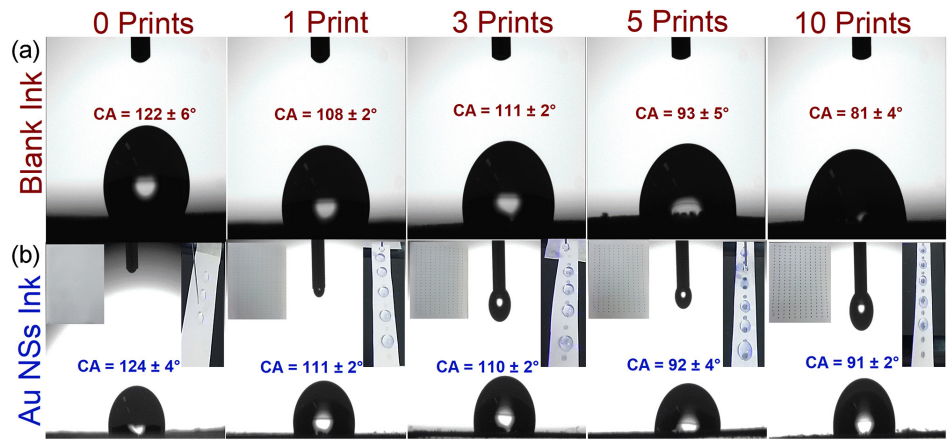

Figure 4. Paper surface hydrophobicity as a function of the CA against the number of printing cycles for (a) blank ink and (b) Au NSs ink. The inset photographs correspond to the real inkjet-printed papers for 1, 3, 5, and 10 prints.

Au NSs SERS substrate performance for detection of DMT

Raman and SERS spectra for DMT neat powder and Au NSs inkjet-printed substrates with and without DMT (10^{-3} mol L^{-1}) were obtained, as shown in Figure 5a. All band assignments are displayed in Table 1.

The Raman spectrum for Au NSs substrate (black spectrum) reveals the presence of the characteristic bands of cellulose[55] at 378, 432, 457, 515, 997, 1027, 1092, 1119, and 1441 cm^{-1}. Most of these bands are overlapped or very close to signals found on the DMT neat powder (dashed lines in Figure 5a) due to the presence of similar vibrations related to C–C, C–H, CH_2, and CH_3 groups present in both molecules. Otherwise, it is important to mention that DMT is a poorly studied molecule, and brief Raman characterization has been found to date.[44] Based on this, for the signal assignment of DMT, we took as a reference previous works reported with similar molecules containing the indole group such as tryptophan,[54,56,57] tryptamine,[54,58] 5-hydroxytryptamine (serotonin),[45,59] and 5-hydroxy *N*,*N*-dimethyltryptamine (bufotenine).[43] The signals at 765, 858, 1003, 1433 and 1548 cm^{-1} in the DMT neat powder correspond with the indole ring breathing + out of plane deformation, δCH out of the plane (pyrrole ring), symmetric ring breathing, indole ring δNH_3^+ in the plane deformation, and indole ring stretching vibration, respectively. Besides, the signals at 1229, 1339, 1351, and 1385 cm^{-1} correspond with the different CH and CH_2 bending modes. Note that the DMT dropped onto Au NSs inkjet-printed surface (blue spectrum) shows a spectral profile slightly different from DMT neat powder. For instance, for bands at 764, 850, 1358, and 1551 cm^{-1} corresponding to the indole ring, there is an intensity decrease in comparison to DMT powder. The signal at 764 cm^{-1} totally disappears at concentrations lower than 10^{-5} mol L^{-1}. In addition, for the signals corresponding to the δCH_2 bending modes at 1230 and 1388 cm^{-1} and the signal at 1124 related to the $\delta N^+H(CH_3)_2$ there is an intensity increase.

These spectral differences are related to the geometrical adsorption of the DMT above the gold surface. As shown in Figure S9, SI section, the analyte can be adsorbed by the interaction of the electron pair on the nitrogen atom of the indole group or by the alkyl amino group in the side chain. This will depend on the charge and type of metal surface (gold or silver), the solution pH that will lead to protonated or deprotonated amine forms, and the molecule concentration.[43,54,56,60] Thus, considering the observed spectral changes in the Raman and SERS spectra and that the DMT solutions were prepared at pH = 5.8 favoring the protonation of the alkyl amino group[43,53] we suggest that the molecule is perpendicularly adsorbed, interacting by the protonated ($-N^+H(CH_3)_2$) group leading to a distortion in the vibrational modes and consequently intensifying the vibrational modes of the CH_2 chain since they are closer to the nanoparticle in comparison to the indole ring (Figure S9a, SI section). Besides, as suggested by Wu *et al.*[43] and da Fonseca *et al.*[56] at low concentrations < 10^{-5} mol L^{-1} there is predominant interaction through the alky lamino side chain. Under this interaction mechanism, the indole group is not interacting directly with the surface as corroborated by the absence of bands at 765, 1358, and the low enhancement at 1581 and 1616 cm^{-1}.

Furthermore, in order to evaluate the performance of Au NSs inkjet-printed substrates to detect DMT in ultralow concentrations, we measured 100 SERS spectra for each concentration between 10^{-3} to 10^{-10} mol L^{-1}, as shown in Figure 5b. Note that the spectral profile for DMT in different concentrations is similar to the spectrum shown in Figure 5a (blue spectrum), and the signal at 1388 cm^{-1} is observed even at 10^{-10} mol L^{-1}, indicating the effective detection of DMT in the lowest concentration.

Table 1. Raman and SERS bands assignments for DMT neat powder, Au NSs-DMT 10^{-3} mol L^{-1}, and Au NSs inkjet-printed

Assignment[43-45,54]	Raman shift / cm^{-1}		
	Raman DMT net powder	SERS Au NSs-DMT 10^{-3} mol L^{-1}	AuNSs inkjet-printed substrate
δ(C–C–C)ring	–	–	378
Skeletal vibrations	–	386	–
γ_{π}(ring)	426	427	–
ν(CCO)ring	–	–	432
δ(ring)/δ(C–N–C)/ν(CCO)ring (cellulose)	459	–	457
δ(ring)/δ(C–C–C)	560	–	–
δ(ring)/δ(C–C–C)	583	595	–
δ(ring)/δ(C–C–C)	726	–	–
γ(CH)/$\rho(CH_2)$	808	–	–
γ(CH)	858	850	–
C–C–C–O/$\rho(CH_3)$	–	–	997
ν(C–N)/δ(C–C–C)	1003	1001	–
Stretching, C–C and C–O	–	–	1027
$\rho(CH_3)$	1068	1068	–
Stretching, C–C and C–O	–	–	1092
ν(C–C)	1096	1096	–
Stretching, C–C and C–O; ν(COC) in plane sym.	–	–	1119
δ(C–H)/$\delta N^{+}H(CH_3)_2$	1123	1124	–
ν(C–N)/$\rho(CH_3)$/$\delta_{tw}(CH_2)$	1174	–	–
δ(C–H)/$\delta_{tw}(CH_2)$	1213	–	–
δ(C–H)/$\delta_{tw}(CH_2)$	1229	1230	–
ν(C–N)/$\rho(CH_3)$	1267	1266	–
$\delta_{tw}(CH_2)$	1311	1311	–
Shoulder	1338	1338	–
ν(ring)	1351	–	–
$\delta_{w}(CH_2)$	1385	1388	–
$\delta_{s}(CH_3)$/$\delta_{sc}(CH_2)$	1433	–	
$\delta_{s}(CH_3)$/$\delta_{sc}(CH_2)$	1453	1446	1441
C–C	1498	–	–
ν(C=C)/ν_{π}(ring)	1548	1551	–
ν(ring)	1577	1581	–
ν_{π}(ring)	1617	1616	–

DMT: *N*,*N*-dimethyltryptamine; SERS: surface-enhanced Raman scattering; Au NSs: gold nanostars.

For better visualization, the statistical analysis projection was performed for the set of SERS spectra displayed in Figure 5b. Initially, the raw dataset at two different power laser intensities (10 and 50%) was analyzed by PCA, as shown in Figures S10 and S11 (SI section). For 10% is possible to observe a tendency towards the formation of clusters for the different concentrations (10^{-3} to 10^{-10} mol L^{-1}) that is slightly clear compared to 50%. However, some clusters overlap, which is reflected in the silhouette coefficient values around 0.08 and 0.34, indicating poor discrimination. After diminishing data dispersion with smooth, denoise, and scattering corrections, the discrimination among sample concentrations becomes clear as depicted in Figure 6. Despite holding 96.93% information, analyzing the data with two principal components, Figure 6a, the tail of 10^{-7} and 10^{-5} mol L^{-1} clusters seem to overlap, but in a 3D point of view, Figure 6b, that is using the third principal component yielding 98.58% of the information, one can observe that 10^{-7} and 10^{-5} mol L^{-1} clusters do not touch each other, reaching a silhouette coefficient of 0.58. The nonlinear IDMAP technique provided a higher coefficient value

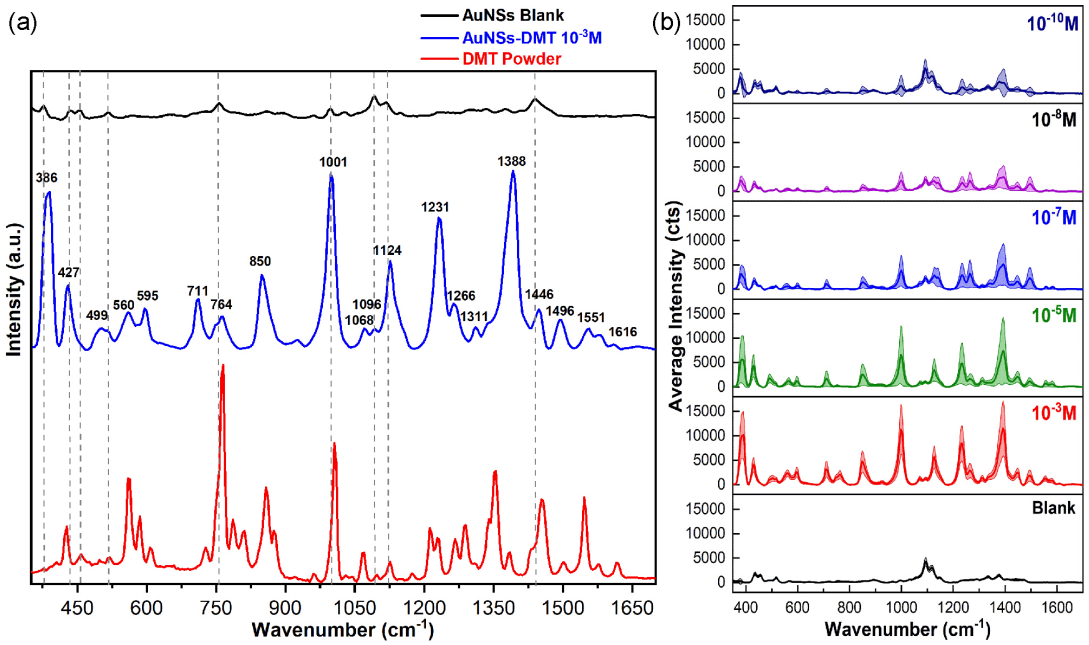

Figure 5. (a) Spectra comparison between DMT neat powder, Au NSs blank, and Au NSs-DMT substrates. (b) Average SERS spectra for the detection of DMT between 10^{-3}-10^{-10} mol L^{-1}.

(0.63) in only two dimensions, which may be due to the nonlinear cluster distribution. Increasing the laser power to 50% enhances the Raman effect, leading to higher intensity thus facilitating data discrimination, that varies linearly with the concentrations, as depicted in Figure 6c, explaining the reason IDMAP projection presents a lower silhouette coefficient value, 0.75, against the PCA (0.84) (Figure S12, SI section). Despite both means that a strong data correlation was obtained with only two principal components. In PCA case, yielding a total of 97.36% of data information, which is similar to the addition of a third principal component, Figure 6d.

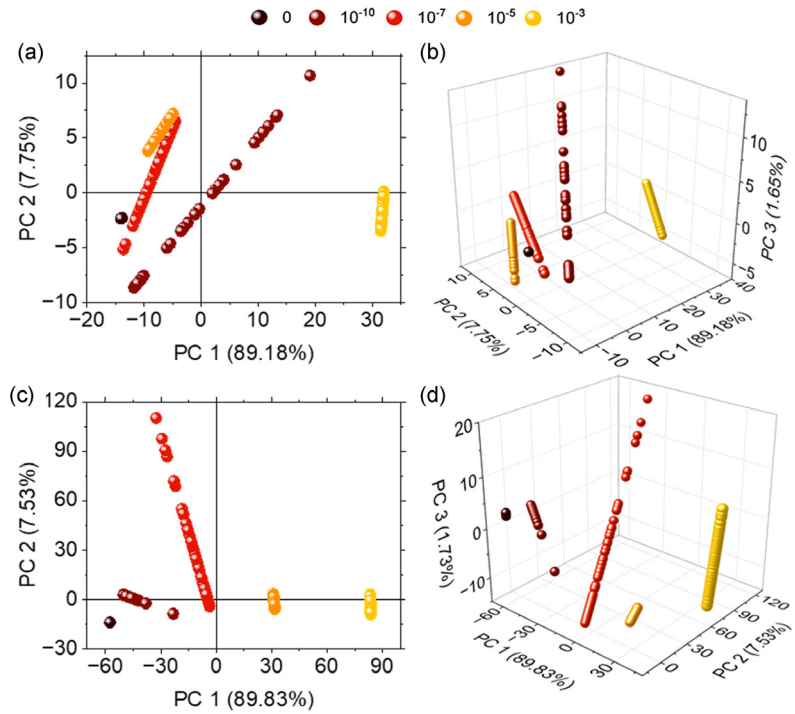

Figure 6. (a) 2D, and (b) 3D PCA scores plot of the whole spectra raw dataset for different concentrations (0, 10^{-10}, 10^{-7}, 10^{-5}, and 10^{-3} mol L^{-1}) for 10% experimental condition. The silhouette coefficient values for 2D and 3D PCA are 0.49 and 0.58, respectively. (c) 2D, and (d) 3D PCA for 50% experimental condition. The silhouette coefficient values for 2D and 3D PCA are 0.84 and 0.83, respectively.

Finally, the reproducibility of the Au NSs inkjet-printed substrates was evaluated using DMT 10^{-5} mol L^{-1}. For this, we measured six different spots by collecting a set of 100 points *per* spot. Note in Figure 7b that the standard deviation of each spot is pretty high, these variations between measures on the same spot are observed because the surface of the Au NSs inkjet-printed substrates is composed of randomly organized fibers; consequently, there are regions with different amounts of nanoparticles, leading to different enhancement intensities. However, when comparing the average SERS intensity between different spots is observed that the results are highly reproducible (Figures 7a-7b). The intensity evaluation demonstrates a low relative standard deviation (RSD) of 17.8% between the average intensity of the 6 analyzed spots. Moreover, the intensity data set was also evaluated considering a deviation range of ±10%, as shown in Figure 7b. The results demonstrate that 80% of the spots present an average intensity in the range of ±10%, validating the reproducibility of spot-to-spot results. This result indicates that the intensity of the SERS peak at 1388 cm^{-1} is a reliable choice for the evaluation of the performance of the SERS substrate as well as for quantification purposes at ultralow concentrations of DMT. This reproducibility evaluation was also performed for CV 10^{-5} mol L^{-1} achieving similar (RSD = 17.4%) results as shown in Figure S13 (SI section).

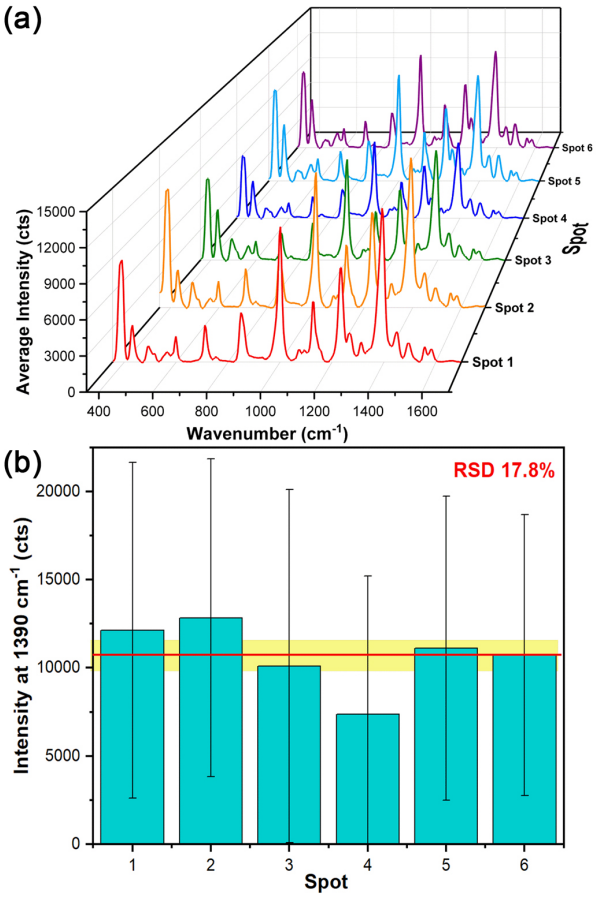

Figure 7. (a) Average SERS spectra and (b) average SERS intensity (1388 cm^{-1}) recorded for DMT 10^{-5} mol L^{-1} measured on 6 different spots printed on three different sheets. The region highlighted in yellow represents a ± 10% intensity variation concerning the average value (red line) for the 6 spots.

Conclusions

In conclusion, the inkjet printing based on flexible paper fabrication using Au NSs and CV as a probe molecule reveals that only one printing cycle with [Au^0] = 27 mmol L^{-1} is enough to achieve the high performance of SERS substrates, compared to the previous work published in our group and the literature for Au nanospheres. This fact could be related to the tips of Au NSs providing an electromagnetic field more efficiently in comparison to other morphologies; consequently, requiring a lower concentration of nanoparticles ink. Additionally, the inkjet-printed paper SERS substrate with Au NSs displayed excellent stability for 90 days in storage conditions of low humidity and protection from light, as well as, great reproducibility among measures for both crystal violet and DMT detection. Finally, the Au NSs inkjet-printing SERS substrates applicability for detection of DMT drug molecules was able to detect up to 10^{-10} mol L^{-1}, and the PCA data reveal high sensitivity and discrimination concentrations with a silhouette coefficient value of 0.84 for 50% of the data used. Therefore, the use of Au NSs combined with the optimized number of printing cycles is the key feature of this work to achieve low DMT detection with high sensitivity, as well as SERS substrates of low cost and easy commercialization. Thus, we hope that this work serves as a first step for developing low-cost, highly sensitive flexible sensors that would help in monitoring the DMT concentration up to the nanomolar range where DMT interacts with serotonin, helping in the study of the role of DMT in the treatment of depression and Alzheimer.

Supplementary Information

Supplementary information is available free of charge at http://jbcs.sbq.org.br as a PDF file.

Acknowledgments

The authors gratefully acknowledge the financial support provided by CNPq (161827/2021-7, 310131/2020-0, 405087/2021-7, 465452/2014-0) FAPESP (2022/02893-1, 2022/11983-4, 2021/02754-9, 2014/50906-9) and CAPES (Finance Code 001) financed PhD Student Edison H.

Montoya. Contributions from the National Nanotechnology Laboratory (LNNano-CNPEM, Brazil) and Multiused Laboratory of Advanced Optical Spectroscopy (LMEOA/IQ-UNICAMP) analysis are also gratefully acknowledged. This contributes to the National Institute of Science and Technology in Complex Functional Materials (CNPq-MCT/FAPESP).

This work is dedicated to Professor Oswaldo Luiz Alves from the Institute of Chemistry- UNICAMP, an esteemed Professor/Researcher in Solid State Chemistry, spectroscopy, and nanoscience, who passed away on July 10th, 2021. The authors acknowledge his immeasurable contributions to science and the lives of those who benefited from his work, wisdom, and unwavering will.

Author Contributions

EHM was responsible for data acquisition, conceptualization, original draft preparation, data curation, validation, writing review and editing; AB for conceptualization, discussion results, writing review and editing; LMFO for data acquisition, review and editing; PACA for data acquisition, review and editing; ALRO for conceptualization, review and editing, funding acquisition; FMS for PCA formal analysis, review and editing; AS for conceptualization, review and editing, funding acquisition FAS for conceptualization, review and editing, funding acquisition; IOM for supervise, conceptualization, writing review and editing, funding acquisition.

References

1. e Amariz, I. A.; da Silva J. P.; de Souza, N. A. C.; Pereira, E. C. V.; Alves, P. A. R.; Santos, V. L. A.; Alencar-Filho, J. M. T.; Nishimura, R. H. V.; Oliveira, A. P.; Rolim-Neto, P. J.; Rolim, L. A.; *Rev. Bras. Farmacogn.* **2022**, *32*, 905. [Crossref]
2. Eckernas, E.; Bendrioua, A.; Cancellerini, C.; Timmermann, C.; Eckern, E.; Carhart-Harris, R.; Hoffmann, K.; Ashton, M.; *J. Pharm. Biomed. Anal.* **2022**, *212*, 114642. [Crossref]
3. Nichols, D. E.; *Pharmacol. Rev.* **2016**, *68*, 264. [Crossref]
4. Barker, S. A.; *Front. Neurosci.* **2018**, *12*, 536. [Crossref]
5. Dunlap, L. E.; Olson, D. E.; Nichols, D. E.; Barker, S. A.; Reckweg, J. T.; Uthaug, M. V.; Szabo, A.; Davis, A. K.; Lancelotta, R.; Mason, N. L.; Ramaekers, J. G.; Chambers, M. I.; Appley, M. G.; Longo, C. M.; Musah, R. A.; Bendrioua, A.; Cancellerini, C.; Timmermann, C.; Eckern, E.; Carhart-harris, R.; Hoffmann, K.; Ashton, M.; Roseman, L.; Schartner, M.; Milliere, R.; Williams, L. T. J.; Erritzoe, D.; Muthukumaraswamy, S.; Ashton, M.; Bendrioua, A.; Kaur, O.; Turton, S.; Nour, M. M.; Day, C. M.; Plaza, G.; Piña, B.; Herrera, H.; Calfuman, K.; Winstock, A. R.; Kaar, S.; Borschmann, R.; Barker, S. A.; Riba, J.; Mcilhenny, E. H.; Bouso, C.; Barker, S. A.; *Pharmacol Rev.* **2022**, *162*, 264. [Crossref]
6. Olson, D. E.; *ACS Pharmacol. Transl. Sci.* **2021**, *4*, 563. [Crossref]
7. Morales-Garcia, J. A.; Calleja-Conde, J.; Lopez-Moreno, J. A.; Alonso-Gil, S.; Sanz-SanCristobal, M.; Riba, J.; Perez-Castillo, A.; *Transl. Psychiatry* **2020**, *10*, 331. [Crossref]
8. Ruscher, K.; Shamloo, M.; Rickhag, M.; Ladunga, I.; Soriano, L.; Gisselsson, L.; Toresson, H.; Ruslim-Litrus, L.; Oksenberg, D.; Urfer, R.; Johansson, B. B.; Nikolich, K.; Wieloch, T.; *Brain* **2011**, *134*, 732. [Crossref]
9. Beaton, J. M.; Morris, P. E.; *Mech. Ageing Dev.* **1984**, *25*, 343. [Crossref]
10. Barker, S. A.; *Psychopharmacology* **2022**, *239*, 1749. [Crossref]
11. Szabó, Í.; Varga, V.; Dvorácskó, S.; Farkas, A. E.; Körmöczi, T.; Berkecz, R.; Kecskés, S.; Menyhárt, Á.; Frank, R.; Hantosi, D.; Cozzi, N. V.; Frecska, E.; Tömböly, C.; Krizbai, I. A.; Bari, F.; Farkas, E.; *Neuropharmacology* **2021**, *192*, 108612. [Crossref]
12. James, E.; Keppler, J.; Robertshaw, T. L.; Sessa, B.; *Hum. Psychopharmacol. Clin. Exp*. **2022**, *37*, e2835. [Crossref]
13. Ryskamp, D. A.; Korban, S.; Zhemkov, V.; Kraskovskaya, N.; Bezprozvanny, I.; *Front. Neurosci.* **2019**, *13*, 862. [Crossref]
14. Griesmaier, E.; Posod, A.; Gross, M.; Neubauer, V.; Wegleiter, K.; Hermann, M.; Urbanek, M.; Keller, M.; Kiechl-Kohlendorfer, U.; *Exp. Neurol.* **2012**, *237*, 388. [Crossref]
15. Szabo, A.; Frecska, E.; *Neural Regen. Res.* **2016**, *11*, 396. [Crossref]
16. Reckweg, J. T.; Uthaug, M. V.; Szabo, A.; Davis, A. K.; Lancelotta, R.; Mason, N. L.; Ramaekers, J. G.; *J. Neurochem.* **2022**, *162*, 128. [Crossref]
17. Riba, J.; Mcilhenny, E. H.; Bouso, C.; Barker, S. A.; *Drug Test Anal.* **2015**, *7*, 401. [Crossref]
18. Dunlap, L. E.; Olson, D. E.; *ACS Omega* **2018**, *3*, 4968. [Crossref]
19. Karila, D.; Freret, T.; Bouet, V.; Boulouard, M.; Dallemagne, P.; Rochais, C.; *J. Med. Chem.* **2015**, *58*, 7801. [Crossref]
20. Rodríguez, L.; López, A.; Moyna, G.; Seoane, G. A.; Davyt, D.; Vázquez, A.; Hernández, G.; Carrera, I.; *ACS Omega* **2022**, *7*, 12307. [Crossref]
21. Plaza, G.; Piña, B.; Herrera, H.; Calfuman, K.; *J. Chil. Chem. Soc*. **2020**, *65*, 4668. [Crossref]
22. Chambers, M. I.; Appley, M. G.; Longo, C. M.; Musah, R. A.; *ACS Omega* **2020**, *5*, 28547. [Crossref]
23. Gaujac, A.; Martinez, S. T.; Gomes, A. A.; de Andrade, S. J.; Pinto, A. C.; David, J. M.; Navickiene, S.; de Andrade, J. B.; *Microchem. J.* **2013**, *109*, 78. [Crossref]
24. Stiles, P. L.; Dieringer, J. A.; Shah, N. C.; Van Duyne, R. P.; *Annu. Rev. Anal. Chem.* **2008**, *1*, 601. [Crossref]
25. Fan, M.; Andrade, G. F. S.; Brolo, A. G.; *Anal. Chim. Acta* **2020**, *1097*, 1. [Crossref]
26. Ji, W.; Li, L.; Zhang, Y.; Wang, X.; Ozaki, Y.; *J. Raman Spectrosc.* **2020**, *52*, 468. [Crossref]

27. Gandra, N.; Portz, C.; Tian, L.; Tang, R.; Xu, B.; Achilefu, S.; Singamaneni, S.; *Angew. Chem., Int. Ed.* **2014**, *53*, 866. [Crossref]
28. Lee, H. K.; Lee, Y. H.; Koh, C. S. L.; Phan-Quang, G. C.; Han, X.; Lay, C. L.; Sim, H. Y. F.; Kao, Y. C.; An, Q.; Ling, X. Y.; *Chem. Soc. Rev.* **2019**, *48*, 731. [Crossref]
29. Phan-Quang, G. C.; Han, X.; Koh, C. S. L.; Sim, H. Y. F.; Lay, C. L.; Leong, S. X.; Lee, Y. H.; Pazos-Perez, N.; Alvarez-Puebla, R. A.; Ling, X. Y.; *Acc. Chem. Res.* **2019**, *52*, 1844. [Crossref]
30. Baena, J. R.; Lendl, B.; *Curr. Opin. Chem. Biol.* **2004**, *8*, 534. [Crossref]
31. Das, R. S.; Agrawal, Y. K.; *Vib. Spectrosc.* **2011**, *57*, 163. [Crossref]
32. Liu, H.; He, Y.; Cao, K.; *Adv. Mater. Interfaces* **2021**, *8*, 2100982. [Crossref]
33. Langer, J.; de Aberasturi, D. J.; Aizpurua, J.; Alvarez-Puebla, R. A.; Auguié, B.; Baumberg, J. J.; Bazan, G. C.; Bell, S. E. J.; Boisen, A.; Brolo, A. G.; Choo, J.; Cialla-May, D.; Deckert, V.; Fabris, L.; Faulds, K.; Javier García de Abajo, F.; Goodacre, R.; Graham, D.; Haes, A. J.; Haynes, C. L.; Huck, C.; Itoh, T.; Käll, M.; Kneipp, J.; Kotov, N. A.; Kuang, H.; Le Ru, E. C.; Lee, H. K.; Li, J. F.; Ling, X. Y.; Maier, S. A.; Mayerhöfer, T.; Moskovits, M.; Murakoshi, K.; Nam, J. M.; Nie, S.; Ozaki, Y.; Pastoriza-Santos, I.; Perez-Juste, J.; Popp, J.; Pucci, A.; Reich, S.; Ren, B.; Schatz, G. C.; Shegai, T.; Schlücker, S.; Tay, L. L.; George Thomas, K.; Tian, Z. Q.; van Duyne, R. P.; Vo-Dinh, T.; Wang, Y.; Willets, K. A.; Xu, C.; Xu, H.; Xu, Y.; Yamamoto, Y. S.; Zhao, B.; Liz-Marzán, L. M.; *ACS Nano* **2020**, *14*, 28. [Crossref]
34. Sui, Y.; Zorman, C. A.; *J. Electrochem. Soc.* **2020**, *167*, 037571. [Crossref]
35. Hoppmann, E. P.; Yu, W. W.; White, I. M.; *Methods* **2013**, *63*, 219. [Crossref]
36. Tay, L.-L.; Poirier, S.; Ghaemi, A.; Hulse, J.; *J. Raman Spectrosc*. **2021**, *52*, 563. [Crossref]
37. Duan, J.; Qiu, Z.; Li, L.; Feng, L.; Huang, L.; Xiao, G.; *Spectrochim. Acta, Part A* **2020**, *243*, 118811. [Crossref]
38. Godoy, N. V.; García-Lojo, D.; Sigoli, F. A.; Pérez-Juste, J.; Pastoriza-Santos, I.; Mazali, I. O.; *Sens. Actuators, B* **2020**, *320*, 128412. [Crossref]
39. Joshi, P.; Santhanam, V.; *RSC Adv.* **2016**, *6*, 68545. [Crossref]
40. Liu, M.; Bhandari, A.; Haqqani Mohammed, M. A.; Radu, D. R.; Lai, C.-Y.; *Appl. Nano* **2021**, *2*, 242. [Crossref]
41. Yu, W. W.; White, I. M.; *Analyst* **2013**, *138*, 1020. [Crossref]
42. Tian, F.; Bonnier, F.; Casey, A.; Shanahan, A. E.; Byrne, H. J.; *Anal. Methods* **2014**, *6*, 9116. [Crossref]
43. Wu, X.; Cañamares, M. V.; Kakoulli, I.; Sanchez-Cortes, S.; *J. Phys. Chem. Lett.* **2022**, *13*, 5831. [Crossref]
44. Vidak, A.; Šapić, I. M.; Dananić, V.; *Integr. Mol. Med.* **2015**, *2*, 354. [Crossref]
45. Do, P. Q. T.; Huong, V. T.; Phuong, N. T. T.; Nguyen, T. H.; Ta, H. K. T.; Ju, H.; Phan, T. B.; Phung, V. D.; Trinh, K. T. L.; Tran, N. H. T.; *RSC Adv.* **2020**, *10*, 30858. [Crossref]
46. Wuithschick, M.; Birnbaum, A.; Witte, S.; Sztucki, M.; Vainio, U.; Pinna, N.; Rademann, K.; Emmerling, F.; Kraehnert, R.; Polte, J.; *ACS Nano* **2015**, *9*, 7052. [Crossref]
47. Ma, J.; Liu, X.; Wang, R.; Zhang, J.; Jiang, P.; Wang, Y.; Tu, G.; *ACS Appl. Nano Mater.* **2020**, *3*, 10885. [Crossref]
48. *Origin(Pro)*, version 2018; OriginLab Corporation, Northampton, MA, USA, 2018.
49. Minghim, R.; Paulovich, F. V.; de Andrade Lopes, A.; *Vis. Data Anal.* **2006**, *6060*, 60600S. [Crossref]
50. Rousseeuw, P. J.; *J. Comput. Appl. Math.* **1987**, *20*, 53. [Crossref]
51. Bär, J.; de Barros, A.; de Camargo, D. H. S.; Pereira, M. P.; Merces, L.; Shimizu, F. M.; Sigoli, F. A.; Bufon, C. C. B.; Mazali, I. O.; *ACS Appl. Mater. Interfaces* **2021**, *13*, 36482. [Crossref]
52. van Rossum, G.; *Python*, Centrum voor Wiskunde en Informatica (CWI), Amsterdam, 1995.
53. Solís, D. M.; Taboada, J. M.; Obelleiro, F.; Liz-Marzán, L. M.; García De Abajo, F. J.; *ACS Photonics* **2017**, *4*, 329. [Crossref]
54. Hussain, S.; Pang, Y.; *J. Mol. Struct.* **2015**, *1096*, 121. [Crossref]
55. Agarwal, U. P.; Ralph, S. A.; Baez, C.; Reiner, R. S.; *Cellulose* **2021**, *28*, 9069. [Crossref]
56. daFonseca, B. G.; Costa, L. A. S.; Sant'Ana, A. C.; *Spectrochim. Acta, Part A* **2018**, *190*, 383. [Crossref]
57. Chuang, C. H.; Chen, Y. T.; *J. Raman Spectrosc.* **2009**, *40*, 150. [Crossref]
58. Gaigalas, A. K.; Reipa, V.; Niaura, G.; *J. Colloid Interface Sci.* **1998**, *203*, 299. [Crossref]
59. Phung, V. D.; Kook, J. K.; Koh, D. Y.; Lee, S. W.; *Dalton Trans.* **2019**, *48*, 16026. [Crossref]
60. Cañamares, M. V.; Pozzi, F.; Lombardi, J. R.; *J. Phys. Chem. C* **2019**, *123*, 9262. [Crossref]

Submitted: March 1, 2024
Published online: June 18, 2024